Nano Research
2021, 14(4): 1069–1077
ISSN 1998-0124 CN 11-5974/O4
https://doi.org/10.1007/s12274-020-3151-8

Research Article

Fe atoms anchored on defective nitrogen doped hollow carbon spheres as efficient electrocatalysts for oxygen reduction reaction

Panpan Su[1,2,§], Wenjuan Huang[1,2,§], Jiangwei Zhang[2,3,§], Utsab Guharoy[2,4], Qinggang Du[1,2], Qiao Sun[4], Qike Jiang[3,5], Yi Cheng[6,7], Jie Yang[1] (✉), Xiaoli Zhang[8], Yongsheng Liu[1], San Ping Jiang[7], and Jian Liu[2,7,9] (✉)

[1] *College of Mathematics and Physics, Shanghai University of Electric Power, Shanghai 200090, China*
[2] *State Key Laboratory of Catalysis, Dalian Institute of Chemical Physics, Chinese Academy of Sciences, Dalian 116023, China*
[3] *Dalian National Laboratory for Clean Energy, Dalian Institute of Chemical Physics, Chinese Academy of Sciences, Dalian 116023, China*
[4] *State Key Laboratory of Radiation Medicine and Protection, Collaborative Innovation Center of Radiation Medicine of Jiangsu Higher Education Institutions, School for Radiological and Interdisciplinary Sciences, Soochow University, Suzhou 215123, China*
[5] *Division of Energy Research Resources, Dalian Institute of Chemical Physics, Chinese Academy of Sciences, Dalian 116023, China*
[6] *Department of Environmental Engineering, School of Metallurgy and Environment, Central South University, Changsha 410083, China*
[7] *WA School of Mines: Minerals, Energy and Chemical Engineering, Curtin University, Perth, WA 6102, Australia*
[8] *State Centre for International Cooperation on Designer Low-Carbon & Environmental Materials, School of Materials Science and Engineering, Zhengzhou University, Zhengzhou 450001, China*
[9] *DICP-Surrey Joint Centre for Future Materials, Department of Chemical and Process Engineering, University of Surrey, Guildford, Surrey, UK*
[§] *Panpan Su, Wenjuan Huang, and Jiangwei Zhang contributed equally to this work.*

Received: 24 June 2020 / **Revised:** 22 September 2020 / **Accepted:** 30 September 2020

ABSTRACT

Defective electrocatalysts, especially for intrinsic defective carbon, have aroused a wide concern owing to high spin and charge densities. However, the designated nitrogen species favorable for creating defects by the removal of nitrogen, and the influence of defects for the coordination structure of active site and oxygen reduction reaction (ORR) activity have not been elucidated. Herein, we designed and synthesized a pair of electrocatalysts, denoted as Fe-N/C and Fe-ND/C for coordination sites of atomic iron-nitrogen and iron-nitrogen/defect configuration embedded in hollow carbon spheres, respectively, through direct pyrolysis of their corresponding hollow carbon spheres adsorbed with $Fe(acac)_3$. The nitrogen defects were fabricated via the evaporation of pyrrolic-N on nitrogen doped hollow carbon spheres. Results of comparative experiments between Fe-N/C and Fe-ND/C reveal that Fe-ND/C shows superior ORR activity with an onset potential of 30 mV higher than that of Fe-N/C. Fe-ND sites are more favorable for the enhancement of ORR activity. Density functional theory (DFT) calculation demonstrates that Fe-ND/C with proposed coordination structure of FeN_{4-x} ($0<x<4$) anchored by OH as axial ligand during ORR, weakens the strong binding of OH* intermediate and promotes the desorption of OH* as rate-determining step for ORR in alkaline electrolyte. Thus, Fe-ND/C electrocatalysts present much better ORR activity compared with that of Fe-N/C with proposed coordination structure of FeN_4.

KEYWORDS

atomic iron, nitrogen defect, coordination environment, hollow carbon spheres, oxygen reduction reaction

1 Introduction

Energy crisis and environmental pollution demands clean energy storage and conversion technologies [1]. Polymer electrolyte membrane fuel cells and metal-air batteries are new-generation energy conversion devices with high energy density which have drawn enormous attention in recent years due to its high efficiency and zero emission [2]. The oxygen reduction reaction (ORR), as a key cathodic reaction, directly affects the output energy capacity of these devices. However, the sluggish kinetics of the multiple proton-couple electron transfer procedures limits the whole efficiency [3]. Although noble-metal catalysts (especially Pt/C catalyst) have demonstrated prominent ORR activity, their high-cost and limited resources have stimulated tremendous efforts to explore precious-metal-free ORR catalysts aiming to substitute noble-metal based catalysts.

During the last few decades, tremendous efforts have been devoted to exploring the alternatives to replace noble-metal-based catalysts from nanoscale engineering to atomic design [4–9]. Among them, atomic transition metal-nitrogen co-doped carbon materials (M-N/C) have aroused widespread attention [10–13]. Latest demonstrations reveal that single metal atoms coordinated with nitrogen forming $M\text{-}N_x$ sites serve as the active centers for ORR, particularly Fe and Co-based catalysts [12, 13]. Strategies to improve the performance of single-atom catalysts are widely investigated such as increasing the density of active sites, enhancing the intrinsic activity of catalyst by the construction of bi-metal or tri-metal active sites or regulation of coordination environment of active sites [6, 14–17]. Introduction of intrinsic defects is identified as effective method to tune the

Address correspondence to Jie Yang, yj_7667@aliyun.com; Jian Liu, jian.liu@curtin.edu.au, jianliu@dicp.ac.cn

coordination structure of single active site [18–21]. Recently, Yao and co-workers demonstrate that defective graphene or carbon capsules with amounts of structural defects provide unique coordination environment for metallic species that exhibits more excellent electrocatalytic activity than that of M-N/C catalysts due to the high spin and charge densities [22–26]. In addition, the defect on Co-N sites co-doped carbon is essential for the formation of Co-N_{4-x} besides of Co-N_4 [27]. Among them, treatment at elevated temperatures is a relatively facile method for nitrogen removal to form vacancy defects. However, the question about which nitrogen species mainly contributed to the defects and the effect of defect for coordination structure of atomic Fe is rarely reported. Thus, it is important to identify the defective sites generated by nitrogen species loss and optimize the coordination environment of atomic Fe to design promising ORR catalysts.

With the aim to disclose the defect sites generated by the evaporation of the nitrogen species, high specific surface area hollow carbon spheres combining the atomic iron active sites coordinated with nitrogen/defects were synthesized and their ORR activities were evaluated. In alkaline electrolyte, iron-nitrogen/defect co-doped hollow carbon spheres (Fe-ND/C) show the higher ORR activity than that of the atomic iron-nitrogen doped hollow carbon spheres (Fe-N/C). As the increase of the defect contents on Fe-ND/C catalysts, the pyrrolic-N evaporation generates new active sites for ORR activities. It means that the defect sites are produced via the evaporation of pyrrolic-N. The enhanced ORR activities of Fe-ND/C verify that Fe-ND as active center are more favorable for ORR than Fe-N.

2 Experimental

2.1 Materials

Tetraethoxysilane (TEOS, 98%), ammonia solution (25%–28%), formaldehyde solution (37 wt.%), N,N-dimethylformamide (DMF) and ethanol were purchased from Sinopharm Chemical Reagent Company. Melamine and Iron(III) 2,4-pentanedionate ($Fe(acac)_3$) were purchased from Aladdin. Pluronic F127 was purchased from sigma. Resorcinol was purchased from Energy chemical. Hydrochloric acid (HCl) and hydrofluoric acid (HF) were purchased from Kemiou Chemical Reagent Company. All of the reagents were of analytical grade and used as received without further purification.

2.2 Preparation of SiO_2@MRF

In a typical experiment, ammonia aqueous solution (NH_4OH, 2.5 mL), absolute ethanol (EtOH, 60 mL) and deionized water (H_2O, 20 mL) were mixed and stirred at the rate of 370 rpm for 30 min at 30 °C. TEOS (2.8 mL) was subsequently added into the mixture dropwise for 30 min and the colorless solution turned white. Afterwards, F127 (0.3 g), resorcinol (1.2 mmol) and formaldehyde solution (0.56 mL) were dissolved into the above white solution and the resulting solution was stirred for 30 min. The melamine (4.8 mmol) and formaldehyde solution (0.42 mL) were injected and stirred for 24 h at 30 °C. After that, a brown solution was obtained and was transferred to a Teflon-lined stainless-steel autoclave, and heated at 100 °C for 24 h. Eventually, the as-obtained precipitate was separated by centrifugation and washed with deionized water and ethanol several times, and dried at 60 °C under vacuum for overnight. The resulting sample was labelled SiO_2@MRF.

2.3 Preparation of N/C and ND/C

SiO_2@MRF was pyrolyzed under N_2 atmosphere in a tube furnace at 700 °C for 3 h with a heating rate of 2 °C·min^{-1} to yield SiO_2@N/C. SiO_2@N/C was then etched by HF (10 wt.%) for 24 h at room temperature to remove SiO_2 template, filtered and dried at 60 °C under vacuum, the obtained sample was labeled N/C. N/C as annealed at 1,050 °C for 2 h with a heating rate of 5 °C·min^{-1} under an atmosphere of nitrogen in order to form defective nitrogen. The resulting sample was denoted as ND/C.

2.4 Preparation of Fe-N/C and Fe-ND/C

The Fe atoms were introduced into the N/C or ND/C via impregnation and heat-treatment followed by acid washing. N/C or ND/C (30 mg), $Fe(acac)_3$ (12.36 mg) were dissolved into DMF (60 mL) by sonication for 1 h. Subsequently, the mixed dispersion solution was heated for 5 h at 80 °C in an oil bath under constant stirring conditions and then was treated by the vacuum rotary evaporation method. The obtained black powder was pyrolyzed at 700 °C for 2 h with a heating rate of 5 °C·min^{-1} under a nitrogen flow in order to stabilize Fe nanoparticles on the supports. Finally, the obtained solid was treated by the way of acid washing with 0.1 M HCl for 5 h at 80 °C accompanied by stirring and vacuum filtration, followed by drying at 60 °C in a vacuum oven overnight. The catalysts were denoted as Fe-N/C and Fe-ND/C, respectively.

2.5 Preparation of Fe-ND/C-*x*

Fe-ND/C was firstly pyrolyzed by heating up at a ramp rate of 5 °C·min^{-1} to the temperature of 900 or 1,100 °C for 2 h under N_2 and then washed by 0.1 M HCl. The obtained samples were named as Fe-ND/C-*x* (*x* = 900, 1,100 °C).

2.6 Material characterization

The scanning electron microscopy (SEM) was detected on FEI Quanta 200F scanning electron microscope operating with a point resolution of 2 nm at 20 kV. The transmission electron microscopy (TEM) was acquired using a HITACHI HT7700 at an acceleration voltage of 100 kV. High resolution transmission electron microscopy (HRTEM) images were recorded on a JEM-F200 microscope. The aberration corrected high-angle annular dark-field scanning transmission electron microscope (AC-HAADF-STEM) images were performed on JEM-2100 at an acceleration voltage of 200 kV. The powder X-ray diffraction (XRD) data was undertaken on a Rigaku D/Max2500PC diffractometer with Cu Kα radiation (λ = 1.5418 Å) over the 2θ range of 5°–80° with a scan speed of 5 °/min at room temperature. X-ray photoelectron spectroscopy (XPS) measurements were performed on an Thermofisher ESCALAB250Xi spectrometer using a monochromated Al Kα X-ray source ($h\nu$ = 1,486.6 eV). All binding energies were referenced to C 1s peak (284.6 eV). Raman measurements were obtained by Renishaw inVia Raman microscope with a 532 nm excitation laser. The elemental analysis of O, N, H were tested on Horiba EMGA-930. The Fe loading was determined using inductively coupled plasma optical emission spectrometry (ICP-OES) on ICPS-8100. N_2 adsorption-desorption isotherms were performed to determine surface areas and pore volumes with a Micromeritics ASAP 2460 apparatus. The X-ray absorption fine structure spectra Fe K-edge were collected at 1W1B beamline of Beijing Synchrotron Radiation Facility (BSRF). The data were collected in fluorescence mode using a Lytle detector while the corresponding reference sample were collected in transmission mode. The samples were ground and uniformly daubed on the special adhesive tape.

2.7 Electrochemical measurement

The electrochemical performance of Fe-N/C catalyst was

measured on the RARSTAT 3000A-DX Bipotentiostat in a three-electrode electrochemical cell, including a rotating ring-disk electrode (RRDE), a platinum wire and Ag/AgCl as the working electrode, counter electrode and reference electrode, respectively. The catalyst ink was prepared by dispersing 5 mg of catalyst powder into mixed solution containing 175 μL of ethanol and 47.5 μL of 5 wt.% Nafion solution, followed by sonication for at least 30 min. Then 7 μL of the homogeneous ink was dropped on the polished glassy carbon (GC) electrode (5.3 mm in diameter) with a Pt ring (catalyst loading: 0.71 mg·cm^{-2}) and dried at the room temperature.

Before testing, 126 mL of 0.1 M KOH solution as the electrolyte in the cell was bubbled with O_2 and N_2 alternately for at least 30 min during the measurement. The cyclic voltammetry (CV) and linear sweep voltammetry (LSV) tests were performed at a scanned rate of 10 mV·s^{-1} in O_2-saturated and N_2-saturated 0.1 M KOH solution under the scan potential ranged from 0.1 to −0.9 V, and the ring electrode potential was set to 1.3 V vs. RHE. LSV measurements were made at different rotation speed from 400 to 2,025 rpm. The corresponding Koutecky-Levich (K-L) plots were chosen at 0.2, 0.3, 0.4, 0.5, 0.6 V in order to fit the electron transfer number (n) from Koutecky-Levich equation

$$\frac{1}{J}=\frac{1}{J_L}+\frac{1}{J_K}=\frac{1}{B\omega^{\frac{1}{2}}}+\frac{1}{J_K}$$

$$B=0.62nFC_0D_0^{\frac{2}{3}}V^{-\frac{1}{6}}$$

where J is the current density, J_K and J_L are the kinetic and limiting current densities, ω is the angular velocity of the disk, n is the electron transfer number, F is the Faraday constant (96,485 C·mol^{-1}), C_0 is the bulk concentration of O_2 (1.2×10^{-6} mol·cm^{-3}), D_0 is the diffusion coefficient of O_2 in 0.1 M KOH (1.9×10^{-5} cm^2·s^{-1}), and V is the kinematic viscosity of the electrolyte (0.01 cm^2·s^{-1}). The constant 0.62 is adopted when the rotating speed is expressed in rad·s^{-1}.

Electron transfer number (n) can be determined by another equation, which follows hydrogen peroxide yield (H_2O_2%)

$$H_2O_2(\%)=200\times\frac{\frac{I_r}{N}}{I_d+\frac{I_r}{N}}$$

$$n=4\times\frac{I_d}{I_d+\frac{I_r}{N}}$$

where I_d is the disk current, I_r is the ring current, and N is the current collection efficiency of the Pt ring (N = 0.37).

3 Results and discussion

Nitrogen doped hollow carbon spheres with core@shell structure (SiO_2@N/C) were prepared by the carbonization of SiO_2@MRF, which was synthesized by a one-pot reaction using a modified Stöber approach by coating SiO_2 with melamine(M)-resorcinol(R)-formaldehyde(F) polymer. In addition, triblock copolymer Pluronic F127 in the experiment was acted as microstructural template. Finally, the SiO_2 core was etched with hydrofluoric acid and the obtained material was denoted as N/C. Nitrogen/defect doped hollow carbon spheres (ND/C) were generated by annealing N/C at 1,050 °C to remove partial nitrogen from N/C in order to form nitrogen vacancies. Subsequently, Fe species modified N/C or ND/C (Fe-N/C or Fe-ND/C) were obtained via impregnation with $Fe(acac)_3$ dissolved in DMF solution, followed by heat-treatment in N_2 atmosphere and acid washing (Scheme 1). SEM and TEM images reveal that SiO_2@MRF (Fig. S1(a) in the Electronic Supplementary Material (ESM)) and SiO_2@N/C (Figs. S1(b) and S1(c) in the ESM) exhibit a core@shell structure with shell thickness of 7 nm. After etching by hydrofluoric acid, a uniform hollow spherical structure was formed on N/C (Fig. S1(d) in the ESM) and ND/C (Fig. S1(e) in the ESM), manifesting their excellent structural robustness during the process of etching SiO_2 and removing heteroatoms. After inducing Fe species, Fe-N/C and Fe-ND/C remain the hollow spherical structure (Fig. S1(f) in the ESM and Figs. 1(a) and 1(b)). In addition, the thicknesses of shell are roughly 7 nm for Fe-ND/C, similar to the thicknesses of shell of ND/C. There are no visible nanoparticles or clusters formed according to AC-HAADF-STEM with subangstrom resolution (Fig. 1(c)), and atomic-scaled dots have been observed on the carbon sphere, revealing the existence of Fe single atoms on ND/C. Moreover, C, N and Fe mapping images of Fe-ND/C (Fig. 1(d)) characterized by HRTEM reveal that Fe and N atoms are uniformly distributed on the prepared hollow carbon spheres. As shown by the powder XRD patterns in Fig. S2 in the ESM, Fe-N/C and Fe-ND/C display only two broad peaks at 24° and 43°, corresponding to the (002) and (100) planes of graphitic carbon [28]. It is confirmed that no diffraction peaks assigned to Fe nanoparticles was observed in the XRD patterns, which is consistent with the results of AC-HAADF-STEM and TEM images.

The further investigation of the surface chemical composition and valence state of Fe-N/C and Fe-ND/C was

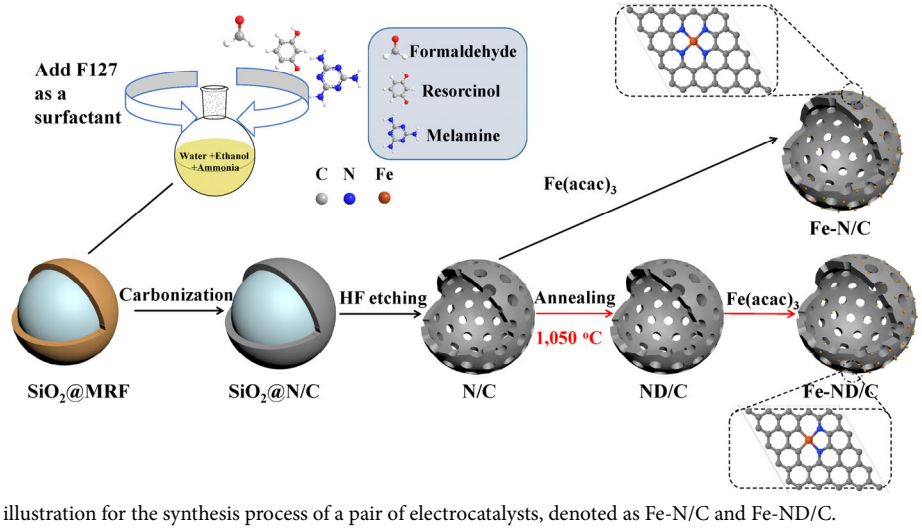

Scheme 1 Schematic illustration for the synthesis process of a pair of electrocatalysts, denoted as Fe-N/C and Fe-ND/C.

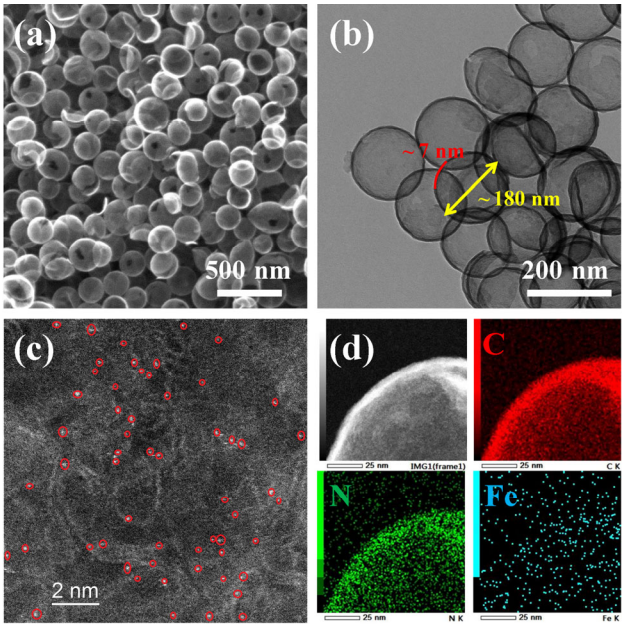

Figure 1 Morphological and structural characterization of the synthesized Fe-ND/C electrocatalysts. (a) SEM, (b) TEM, (c) AC-HAADF-STEM images. The Fe single atoms are marked with red circles. (d) HAADF-STEM image and corresponding EDX element mappings: C (red), N (green), Fe (blue).

measured by XPS. The nature of the surface nitrogen species was analyzed and the result is shown in Fig. 2(a). The N 1s XPS spectra of Fe-N/C and Fe-ND/C can be fitted into three states at 401.2, 400.2, and 398.3 eV, which is ascribed to graphitic-N, pyrrolic-N and pyridinic-N, respectively [29]. The three nitrogen species provide different electronic environment for contiguous carbon atoms, resulting in different electrocatalytic activity [20]. The intensity of N 1s peak for Fe-N/C catalyst decreased obviously after annealing at 1,050 °C. This observation can be verified by the elemental analysis (Table S1 in the ESM). Furthermore, high temperature calcination has great impact on nitrogen species. It should be noted that for Fe-ND/C the nitrogen species were mainly consisted of graphitic and pyridinic-N, which are considered to serve as anchoring sites of Fe atoms. The relative content of graphitic-N for Fe-ND/C is higher than Fe-N/C, while the content of pyrrolic-N is extremely less than Fe-N/C and pyridinic-N has no obvious decrease, suggesting most of the defect sites are generated from the evaporation of relatively unstable pyrrolic-N [30]. As shown in Fig. 2(b), the absolute content of graphitic-N remains unchanged.

The degree of defects and graphitization of carbon catalysts were investigated by Raman spectroscopy. Raman spectra clearly exhibit the variation of the intensity of D and G bands at 1,350 and 1,590 cm^{-1} [31], respectively, both for Fe-N/C and Fe-ND/C (Fig. 2(c)). D band represents the defects and disorders of carbon. G band is attributed to graphitic carbon. Thus, the intensity ratio of D band and G band (I_D/I_G) could be a criterion for the degree of defect. The formation of nitrogen vacancies can enhance the degree of catalyst defect. The I_D/I_G value of Fe-ND/C (0.97) is much higher than Fe-N/C (0.85), indicating the formation of defects on Fe-ND/C, which coincides well with the results of XPS spectra.

The Fe loadings of samples were determined by ICP-OES. For Fe-ND/C and Fe-N/C catalysts, Fe content is 0.12 and 0.27 (wt.%), respectively. Because of the very low Fe content, the Fe 2p signal of Fe-ND/C and Fe-N/C is very weak (Fig. 2(d)). The binding energies of Fe 2p peak for Fe-ND/C and Fe-N/C are around 711.2 eV (Fe $2p_{3/2}$) and 724.5 eV (Fe $2p_{1/2}$) [32], respectively, indicating the presence of Fe^{3+} species. The Fe^{3+} species should be coordinated by vacancy sites and nitrogen species. Fe content of Fe-ND/C rich of vacancy sites is ~ 50% lower than that of Fe-N/C (Table S1 in the ESM), which may be contributed to the lower coordination interaction of defect sites with Fe ions (Fe-D) than that of nitrogen species with Fe ions (Fe-N).

The valance state and coordination environment of the iron in Fe-ND/C were further characterized using X-ray absorption fine structure (XAFS). Figure 2(e) shows the Fe-K X-ray absorption near-edge structure (XANES) spectra for Fe-ND/C and the reference samples. The XANES absorption edge corresponding to 1s to 4p transitions for Fe-ND/C was located at 7,110 eV, which is the same with that for Fe(III)-phthalocyanine. This result indicated that the Fe (III) valence state was dominant in Fe-ND/C, which is consistent with XPS results. The coordination environment of the iron was analyzed by extended X-ray absorption fine structure (EXAFS) in radial distance $\chi(R)$ spectra (Fig. 2(f)), Fe-ND/C exhibits one notable

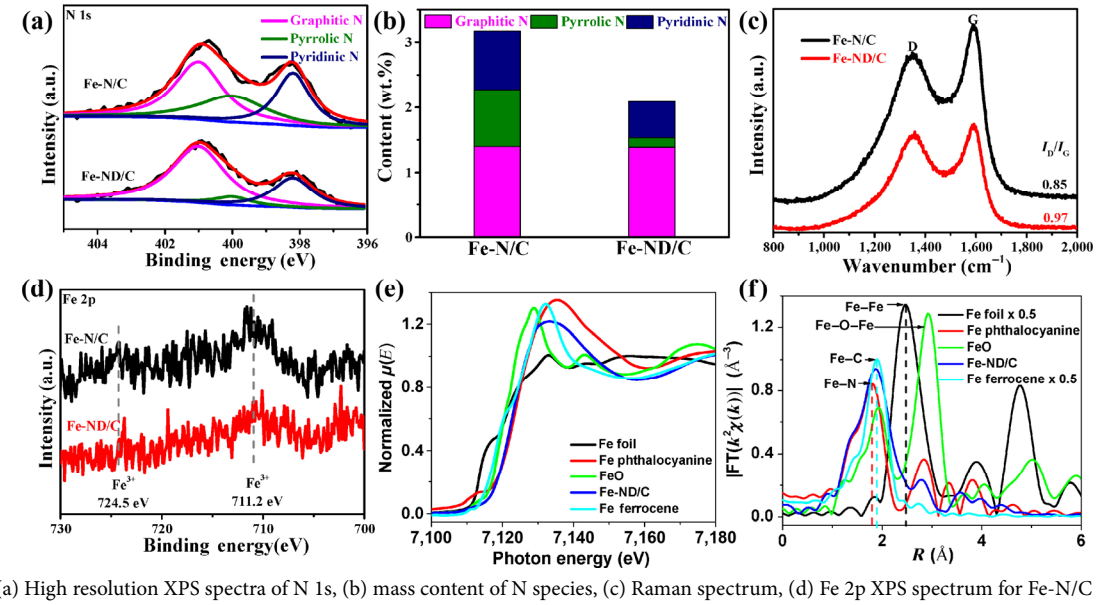

Figure 2 (a) High resolution XPS spectra of N 1s, (b) mass content of N species, (c) Raman spectrum, (d) Fe 2p XPS spectrum for Fe-N/C and Fe-ND/C catalysts, (e) The normalized XANES $\mu(E)$ spectra and (f) The k_2-weighted Fourier transform of EXAFS in radial distance $\chi(R)$ spectra at the Fe K-edge for Fe foil, Fe phthalocyanine, FeO, Fe-ND/C and Fe ferrocene

peak at 1.87 Å, which is in between that for Fe–C (1.90 Å) and Fe–N (1.81 Å). Thus, Fe species may be heterozygous coordinated with nitrogen and carbon. Moreover, the absence of Fe-Fe bond (2.48 Å) and Fe–O–Fe bond (2.91 Å) indicated the Fe species exist as atomically dispersed in Fe-ND/C, which is consistent with HRTEM result. EXAFS fitting shows that Fe atom on Fe-ND/C was coordinated with two carbon and two nitrogen atoms and one OH group (Fig. S3 and Table S2 in the ESM).

The electrocatalytic performance of the prepared catalysts for ORR was evaluated in O_2 or N_2-saturated 0.1 M KOH aqueous electrolyte via CV and LSV at a scan rate of 10 mV·s^{-1}. No redox-peaks was observed on both catalysts in the N_2 bubbled electrolyte, an obvious cathodic peak appeared for each CV curve in O_2 bubbled electrolyte (Fig. 3(a)), indicating an effective ORR. The fluctuation of the CV curves in O_2 bubbled electrolyte is caused by the slow diffusion of oxygen under resting state [33]. The curve of Fe-ND/C shows a cathodic peak for ORR at 0.79 V vs. RHE which is more positive than that of Fe-N/C (0.75 V vs. RHE), indicating the better ORR electrochemical activity than Fe-N/C. The LSV curves (Fig. 3(b)) further demonstrate the catalytic performance of Fe-ND/C at a rotation rate of 1,600 rpm. Impressively, the onset potential and half-wave potential of Fe-ND/C are measured to be 0.91 and 0.79 V vs. RHE, respectively, which are higher than those of Fe-N/C (0.88 and 0.76 V vs. RHE), revealing higher electrocatalytic activity of Fe-ND/C. The half-wave potential of Fe-ND/C was compared with previously reported Fe-based catalyst and listed in Table S3 in the ESM. Apart from this, the onset potential of Fe-N/C and Fe-ND/C are more positive than those of the corresponding N/C (0.84 vs. RHE) and ND/C (0.86 V vs. RHE) shown in the Fig. S4 in the ESM, indicating Fe-N or Fe-ND sites on Fe-N/C and Fe-ND/C are active centers to catalyze ORR. The iron content on Fe-ND/C was tuned, while original Fe-ND/C shows the highest ORR activity (Fig. S5 in the ESM), which indicated that the structure not quantity of active site determines ORR activity. Furthermore, at the potential of 0.7 and 0.8 V vs. RHE (Fig. 3(c)), the current density of Fe-ND/C is higher than that of Fe-N/C, signifying that Fe-ND sites are more favorable than Fe-N sites for the boosted ORR activity, which means the pyrrolic-N evaporation generate new active sites for ORR activity. The high intrinsic ORR activity of Fe-ND/C can be further verified by the smaller Tafel slope of 73.4 mV·dec^{-1} compared with that of Fe-N/C (88.7 mV·dec^{-1}). In order to further investigate the influence of surface area of synthesized catalysts for ORR activity, N_2 adsorption-desorption isotherms were used to analyze the specific surface area and porous structure of Fe-N/C, Fe-ND/C and their corresponding carbon support (N/C and ND/C) (Fig. S6 and Table S4 in the ESM). The type IV isotherms with a distinct hysteresis loop in the P/P_0 range of 0.4–1.0 were found for all samples, indicating a micro/meso porous structure and a large specific surface area [34]. The surface area of Fe-ND/C is 387 m^2·g^{-1}, which is similar to that of Fe-N/C (394 m^2·g^{-1}) (Fig. S6 in the ESM). However, the textural properties of Fe-N/C (S_{BET}: 394 m^2·g^{-1}; V_{micro}: 0.08 cm^3·g^{-1}) and Fe-ND/C (S_{BET}: 387 m^2·g^{-1}; V_{micro}: 0.04 cm^3·g^{-1}) are inferior to N/C (S_{BET}: 630 m^2·g^{-1}; V_{micro}: 0.17 cm^3·g^{-1}) and ND/C (S_{BET}: 657 m^2·g^{-1}; V_{micro}: 0.13 cm^3·g^{-1}), respectively, strongly demonstrating that Fe species which occupied microchannel partially have modified N/C or ND/C with increased graphitic degree [35]. Therefore, combined with the results of textural properties and ORR activity, the change in activity of all catalysts could be attributed to the activity variation of each active center rather than the difference in specific surface area.

The ORR kinetics of Fe-ND/C catalyst could be illustrated by LSV curves at different rotation rates during 400–2,025 rpm (Fig. 4(a)). As the increase of rotation rates, the current densities increase because of the enhanced gas diffusion [36]. The corresponding Koutecky-Levich (K-L) plots (J^{-1} vs. $\omega^{-1/2}$) for Fe-ND/C (Fig. 4(b)), fitted at various electrode potentials from Fig. 4(a), present good linearity and parallelism, suggesting a first-order reaction involved with dissolved oxygen concentration and a potential-independent electron transfer rate [37]. Based on the slope of K-L plots, the transferred electron number (n) per oxygen molecule in ORR was calculated as 4.2–4.3 between −0.3 to −0.6 V via K-L equation, demonstrating a four-electron transfer process over single active site. It also has been confirmed by RRDE measurements. The n value of Fe-ND/C is 3.9–4.0 and the molar ratio of generated H_2O_2 to H_2O is

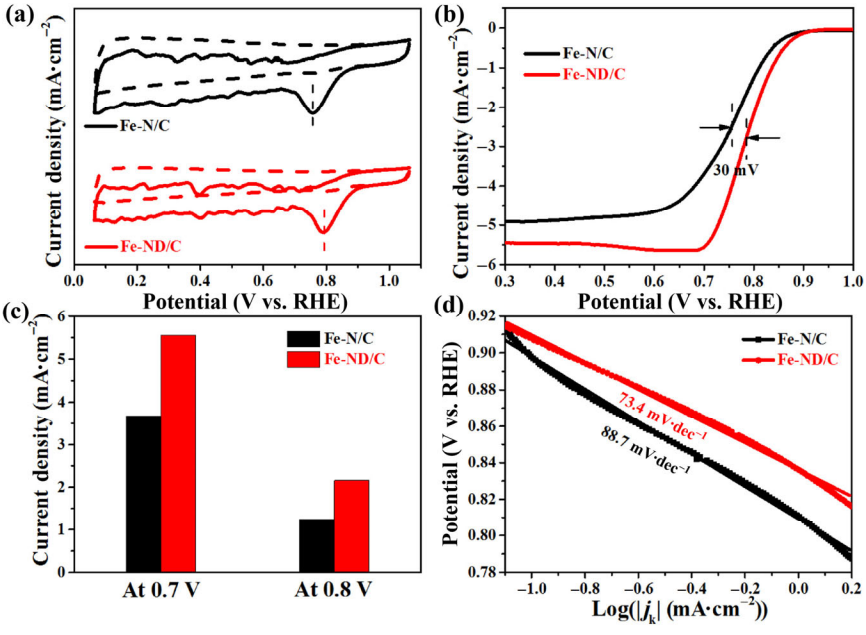

Figure 3 (a) CV curves for the as-prepared samples in O_2 (solid line) or N_2 (dash line) bubbled 0.1 M KOH at a scan rate of 10 mV·s^{-1}. (b) LSV curves for Fe-N/C and Fe-ND/C catalysts in O_2 bubbled 0.1 M KOH at a rotation rate of 1,600 rpm with a scan rate of 10 mV·s^{-1}, (c) current density of Fe-N/C and Fe-ND/C catalysts for ORR at 0.7 and 0.8 V vs. RHE, respectively, and (d) Tafel plots of Fe-N/C and Fe-ND/C.

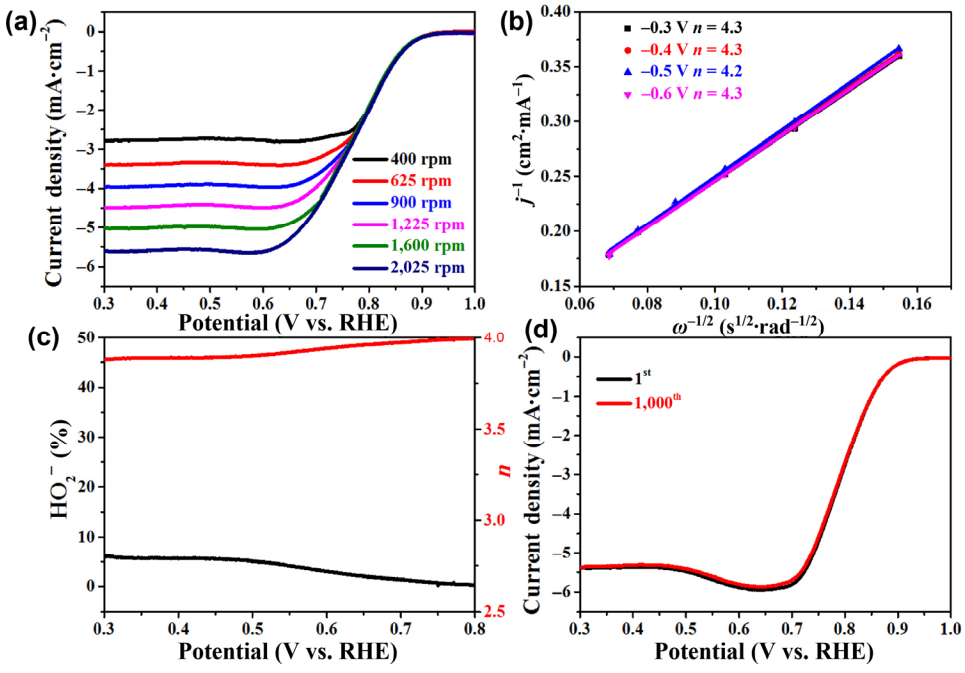

Figure 4 (a) LSV curves of Fe-ND/C catalyst in O_2 bubbled 0.1 M KOH at different rotation rates, (b) K-L plots of Fe-ND/C at the potential range of −0.3 to −0.6 V vs. RHE, (c) the H_2O_2 yield and electron transfer number (n) on per O_2 molecular versus potential curve for Fe-ND/C, and (d) 1st and 1,000th LSV curves of Fe-ND/C in O_2 bubbled 0.1 M KOH at 1,600 rpm.

below 6% within 0.3–0.8 V (Fig. 4(c)), while n and the H_2O_2 yield of Fe-N/C is 3.75–3.95 and above 10% within 0.3–0.8 V (Fig. S7 in the ESM), providing the evidence that the pyrrolic-N evaporation can definitely promote the ORR activity of Fe-N/C by reducing the production of H_2O_2. Furthermore, durability is considered as the other key factor to evaluate the property of catalysts in general. The long-term stability of the Fe-ND/C was investigated by LSV after the accelerated durability tests (ADT). A negligible decay in half-wave potential of Fe-ND/C was observed after 1,000 cycles (Fig. 4(d)), revealing a stable LSV performance. In addition, chronoamperometric (CA) tests were performed in O_2 bubbled 0.1 M KOH solution at 0.5 V vs. RHE to further verify the excellent stability of the Fe-ND/C. Fe-ND/C could maintain 90.7% of its initial current after running for 18,000 s (Fig. S8 in the ESM).

To make a deep insight to the influence of defect contents of Fe-ND/C on the ORR activity, Fe-ND/C catalyst was pyrolyzed at different temperatures under a N_2 atmosphere followed by acid washing. The resulting samples were denoted as Fe-ND/C-x (x = 900, 1,100 °C). ICP result demonstrates that the Fe contents of Fe-ND/C-x are lower than that of Fe-ND/C (0.12 wt.%), indicating that partial Fe atoms aggregated into Fe particle at high temperature and then were leached by acid washing. The similar Fe content (0.07 wt.%) of Fe-ND/C-x suggests that the rest Fe species exist as isolated atoms and show strong thermal stability. As shown in the Table S1 in the ESM, the N content decreases monotonically with the increase of the pyrolysis temperature, demonstrating the number of nitrogen vacancies increases with the increase of temperature. With the similar content of Fe, the catalysts with lower N content display more excellent ORR activity (Fig. S9 in the ESM). Especially for Fe-ND/C-1,100 with 1.05 wt.% of N, it shows the highest onset potential (0.94 V vs. RHE) among the tested samples, which is attributed to the presence of more nitrogen defects and the thermally stable Fe single atoms [38]. Therefore, as the increase of the defect contents on Fe-ND/C catalysts, the pyrrolic-N evaporation generates new active sites for ORR activities.

In order to reveal the origin of the superior ORR activity on Fe-ND/C than Fe-N/C, first-principles density functional theory (DFT) computations were conducted to address the influence of nitrogen vacancies on the activity for ORR. For a systematic investigation of the ORR performance of Fe-N-C catalyst in an alkaline media, both the active sites of various Fe-N/C anchored with possible reaction intermediates and clean Fe-N/C surfaces have been proposed. The models of FeN_4, FeN_3 and FeN_2, and corresponding structures anchored with OH (denoted as FeN_2-OH, FeN_3-OH, FeN_4-OH) are used for theoretical calculations. Geometric structures of FeN_4-OH, FeN_3-OH and FeN_2-OH are shown in Figs. 5(a)–5(c). The ORR process in the alkaline electrolyte, includes the O_2 hydrogenation to OOH*, O–O bond scission of OOH* to O*, protonation of O* to OH*, and OH* removal to form OH^-, corresponding free energy diagram are calculated and shown in Fig. 5(d). At 0.455 V equilibrium potential in alkaline media, all the catalyst models showcase a similar trend of OOH* → O* reaction step to be exothermic, while other steps are endothermic on three kind of catalyst models. The OH* desorption reaction step is found to be the rate-determining step (RDS) and corresponding endothermicity presents the following trend from low to high: FeN_2-OH (0.42 eV) < FeN_3-OH (0.52 eV) < FeN_4-OH (0.55 eV). Compared with FeN_4-OH catalysts, FeN_2-OH and FeN_3-OH models, weaken the strong binding of OH* intermediate, thereby promoting better desorption of OH* binding on the surface. For comparisons, geometric structures of FeN_4, FeN_3 and FeN_2 are shown in Figs. S10(a)–S10(c) in the ESM, corresponding free energy diagram of the successive steps of formation of OOH*, O*, OH*, and desorption of OH* are calculated and shown in Fig. S11 in the ESM. The OH desorption step on FeN_4, FeN_3 and FeN_2 is still the RDS, as the same with FeN_2-OH, FeN_3-OH, FeN_4-OH. The endothermicity presents the following trend from low to high: FeN_4 (0.68 eV) < FeN_3 (0.76 eV) < FeN_2 (0.92 eV), all of these values are much higher than that on catalyst surfaces with OH ligand. Thus, catalyst with OH binding maybe as the real active site to catalyze ORR, and the ORR activity of active site FeN_{4-x}-OH is higher than FeN_4-OH. For Fe-N/C catalyst, the active site is widely imaged as FeN_4. Combing the experimentally superior

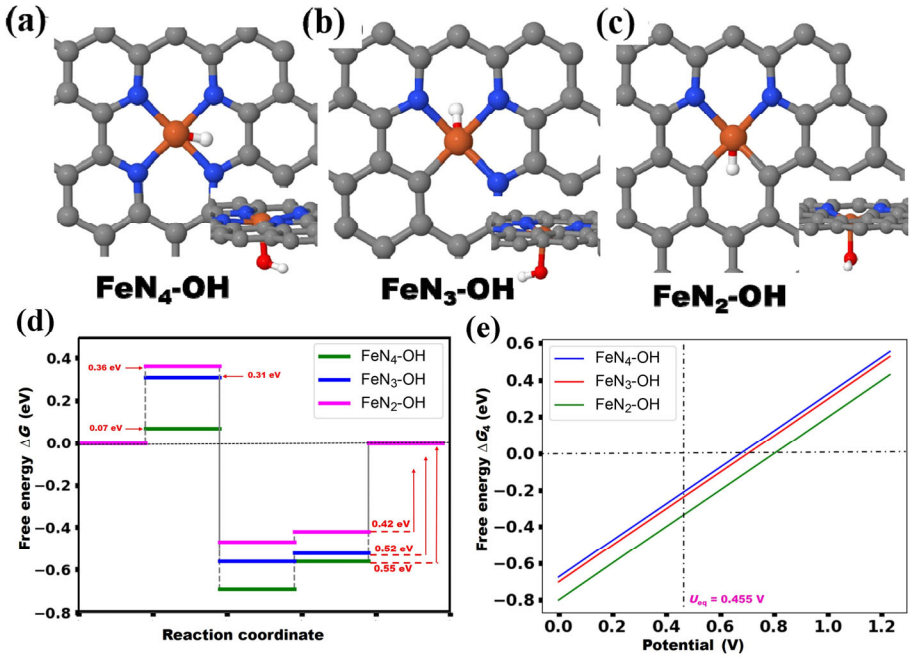

Figure 5 (a)–(c) Front bottom views of FeN_4, FeN_3, FeN_2 structures with OH ligand. The grey, blue, orange, red and white atoms represent C, N, Fe, O and H atoms respectively. (d) The free energy profiles of FeN_x with OH ligand structures for ORR mechanism at 0.455 V equilibrium potential in alkaline media. (e) Free energy of $OH^* \rightarrow OH^-$ as function of electrode potential.

activity of Fe-ND/C than Fe-N/C, the active site of Fe-ND/C are proposed as FeN_{4-x}. In order to explore the defect influence for ORR activity, FeN_2-D with defect sites model was calculated (Fig. S12 in the ESM). The OH desorption step on FeN_2-D is the RDS, as the same with FeN_2, and FeN_2-D presents the lower endothermicity than FeN_2. Thus, FeN_2-D catalyst with defect site shows the high ORR activity than that of FeN_2.

Furthermore, to understand the influence of electrode potential on the RDS reaction step for the considered Fe-N-C surfaces, a free energy plot for $OH^* \rightarrow OH^-$ reaction step during electrode potential (0–1.23) V has been drawn in Fig. 5(e). In particular, $OH^* \rightarrow OH^-$ reaction step for FeN_2-OH becomes exergonic at ~ 0.8 V vs. RHE, which essentially consistent with the onset potential toward ORR at Fe-ND-C. In contrast, $OH^* \rightarrow OH^-$ reaction step for FeN_4-OH is still endothermic at 0.8 V. At equilibrium electrode potential (U_{eq} = 0.455 V), the FeN_2-OH and FeN_3-OH showcase the much higher exergonic than FeN_4-OH surface, indicating FeN_2-OH and FeN_3-OH presenting higher ORR activity than that of FeN_4-OH. Therefore, it can be concluded that lower Fe-N coordination combined with an OH ligand (FeN_2-OH) showcases the best ORR activity, which corresponds to the experimental result about the superior activity of Fe-ND-C than Fe-N-C. The OH-ligand on catalyst surfaces will behave as active site towards the ORR intermediates and represents a reliable method of ascertaining the performance of catalyst surfaces for ORR.

4 Conclusions

In summary, a pair of electrocatalysts, namely, atomic iron-nitrogen and iron-nitrogen/defect modified hollow carbon spheres (Fe-N/C and Fe-ND/C) were successfully synthesized by pyrolysis of $Fe(acac)_3$ in the presence of their corresponding hollow carbon spheres. The defect sites are mainly generated via the evaporation of pyrrolic-N on nitrogen doped hollow carbon spheres. The loading amount of atomic iron on Fe-ND/C is ~ 50% lower than that of Fe-N/C, indicating coordination interaction of atomic Fe with ND-C is weaker than that with N-C. Thus, the electronic state of iron affected by coordination environment on Fe-ND/C is different from Fe-N/C, which determine the ORR activity. In alkaline electrolyte, Fe-ND/C shows much higher ORR activity than that of Fe-N/C, revealing that defect sites generated from the pyrrolic-N evaporation are beneficial for promoting ORR activities. DFT calculations identify that Fe-ND/C catalyst coordinated with OH ligand is the real active site during ORR process, which weakens the strong binding of OH* intermediate, thereby promoting better desorption of OH* binding on the catalyst. Therefore, the ORR activity of Fe-ND-C with nitrogen defect significantly improves compared to that on Fe-N-C without nitrogen vacancies. Thus, comparing to Fe-N sites, Fe-ND sites are more favorable for the enhancement of ORR activity. We believe our findings will provide novel insights for designing electrocatalysts with more pyrrolic-N vacancies and fundamental understanding of electrocatalytic reactions with atomic clusters catalysts.

Acknowledgements

This work was supported financially by the National Natural Science Foundation of China (Nos. 21905271 and 21701168), Liaoning Natural Science Foundation (Nos. 20180510029, 20180510043, and 20180510050), the Dalian National Laboratory for Clean Energy (DNL), CAS, DNL Cooperation Fund, CAS (No. DNL180402), and Australian Research Council (No. DP180100568). For XAFS measurement, we gratefully acknowledge 1W1B beamline of Beijing Synchrotron Radiation Facility (BSRF) Beijing, China for providing the beam time.

Electronic Supplementary Material: Supplementary material (TEM imaging, XRD patterns, LSV curves of N/C, DN/C, H_2O_2 yield and DFT calculation method) is available in the online version of this article at https://doi.org/10.1007/s12274-020-3151-8.

References

[1] Wang, S. Y.; Jiang, S. P. Prospects of fuel cell technologies. *Natl. Sci. Rev.* **2017**, *4*, 163–166.

[2] Cheng, Y.; He, S.; Lu, S. F.; Veder, J. P.; Johannessen, B.; Thomsen, L.; Saunders, M.; Becker, T.; De Marco, R.; Li, Q. F. et al. Iron single atoms on graphene as nonprecious metal catalysts for high-temperature polymer electrolyte membrane fuel cells. *Adv. Sci.* **2019**, *6*, 1802066.

[3] Kuang, M.; Wang, Q. H.; Han, P.; Zheng, G. F. Cu, Co-embedded N-enriched mesoporous carbon for efficient oxygen reduction and hydrogen evolution reactions. *Adv. Energy Mater.* **2017**, *7*, 1700193.

[4] Wang, X. Q.; Li, Z. J.; Qu, Y. T.; Yuan, T. W.; Wang, W. Y.; Wu, Y.; Li, Y. D. Review of metal catalysts for oxygen reduction reaction: From nanoscale engineering to atomic design. *Chem* **2019**, *5*, 1486–1511.

[5] Wang, A. Q.; Li, J.; Zhang, T. Heterogeneous single-atom catalysis. *Nat. Rev. Chem.* **2018**, *2*, 65–81.

[6] Chen, M. J.; He, Y. H.; Spendelow, J. S.; Wu, G. Atomically dispersed metal catalysts for oxygen reduction. *ACS Energy Lett.* **2019**, *4*, 1619–1633.

[7] Xia, W.; Mahmood, A.; Liang, Z. B.; Zou, R. Q.; Guo, S. J. Earth-abundant nanomaterials for oxygen reduction. *Angew. Chem., Int. Ed.* **2016**, *55*, 2650–2676.

[8] Xu, Q.; Guo, C. X.; Tian, S. B.; Zhang, J.; Chen, W. X.; Cheong, W. C.; Gu, L.; Zheng, L. R.; Xiao, J. P.; Liu, Q. et al. Coordination structure dominated performance of single-atomic Pt catalyst for anti-Markovnikov hydroboration of alkenes. *Sci. China Mater.* **2020**, *63*, 972–981.

[9] Tong, Y. Y.; Guo, H. P.; Liu, D. L.; Yan, X.; Su, P. P.; Liang, J.; Zhou, S.; Liu, J.; Lu, G. Q.; Dou, S. X. Vacancy engineering of iron-doped $W_{18}O_{49}$ nanoreactors for low-barrier electrochemical nitrogen reduction. *Angew. Chem., Int. Ed.* **2020**, *59*, 7356–7361.

[10] Pan, Y.; Lin, R.; Chen, Y. J.; Liu, S. J.; Zhu, W.; Cao, X.; Chen, W. X.; Wu, K. L.; Cheong, W. C.; Wang, Y. et al. Design of single-atom Co-N_5 catalytic site: A robust electrocatalyst for CO_2 reduction with nearly 100% CO selectivity and remarkable stability. *J. Am. Chem. Soc.* **2018**, *140*, 4218–4221.

[11] Sun, T. T.; Zhao, S.; Chen, W. X.; Zhai, D.; Dong, J. C.; Wang, Y.; Zhang, S. L.; Han, A. J.; Gu, L.; Yu, R. et al. Single-atomic cobalt sites embedded in hierarchically ordered porous nitrogen-doped carbon as a superior bifunctional electrocatalyst. *Proc. Natl. Acad. Sci. USA* **2018**, *115*, 12692–12697.

[12] Zhang, L. Z.; Fischer, J. M. T. A.; Jia, Y.; Yan, X. C.; Xu, W.; Wang, X. Y.; Chen, J.; Yang, D. J.; Liu, H. W.; Zhuang, L. Z. et al. Coordination of atomic Co-Pt coupling species at carbon defects as active sites for oxygen reduction reaction. *J. Am. Chem. Soc.* **2018**, *140*, 10757–10763.

[13] Zhu, C. Z.; Shi, Q. R.; Xu, B. Z.; Fu, S. F.; Wan, G.; Yang, C.; Yao, S. Y.; Song, J. H.; Zhou, H.; Du, D. et al. Hierarchically porous M-N-C (M = Co and Fe) single-atom electrocatalysts with robust MN_x active moieties enable enhanced ORR performance. *Adv. Energy Mater.* **2018**, *8*, 1801956.

[14] Shen, H. J.; Gracia-Espino, E.; Ma, J. Y.; Tang, H. D.; Mamat, X.; Wagberg, T.; Hu, G. Z.; Guo, S. J. Atomically FeN_2 moieties dispersed on mesoporous carbon: A new atomic catalyst for efficient oxygen reduction catalysis. *Nano Energy* **2017**, *35*, 9–16.

[15] Li, X. Y.; Rong, H. P.; Zhang, J. T.; Wang, D. S.; Li, Y. D. Modulating the local coordination environment of single-atom catalysts for enhanced catalytic performance. *Nano Res.* **2020**, *13*, 1842–1855.

[16] Ding, R.; Liu, Y. D.; Rui, Z. Y.; Li, J.; Liu, J. G.; Zou, Z. G. Facile grafting strategy synthesis of single-atom electrocatalyst with enhanced ORR performance. *Nano Res.* **2020**, *13*, 1519–1526.

[17] Li, Y. C.; Liu, X. F.; Zheng, L. R.; Shang, J. X.; Wan, X.; Hu, R. M.; Guo, X.; Hong, S.; Shui, J. L. Preparation of Fe-N-C catalysts with FeN_x (x=1, 3, 4) active sites and comparison of their activities for the oxygen reduction reaction and performances in proton exchange membrane fuel cells. *J. Mater. Chem. A* **2019**, *7*, 26147–26153.

[18] Zhang, Y. Q.; Guo, L.; Tao, L.; Lu, Y. B.; Wang, S. Y. Defect-based single-atom electrocatalysts. *Small Methods* **2019**, *3*, 1800406.

[19] Xie, C.; Yan, D. F.; Chen, W.; Zou, Y. Q.; Chen, R.; Zang, S. Q.; Wang, Y. Y.; Yao, X. D.; Wang, S. Y. Insight into the design of defect electrocatalysts: From electronic structure to adsorption energy. *Mater. Today* **2019**, *31*, 47–68.

[20] Yan, X. C.; Jia, Y.; Yao, X. D. Defects on carbons for electrocatalytic oxygen reduction. *Chem. Soc. Rev.* **2018**, *47*, 7628–7658.

[21] Yan, D. F.; Li, Y. X.; Huo, J.; Chen, R.; Dai, L. M.; Wang, S. Y. Defect chemistry of nonprecious-metal electrocatalysts for oxygen reactions. *Adv. Mater.* **2017**, *29*, 1606459.

[22] Zhang, L. Z.; Jia, Y.; Gao, G. P.; Yan, X. C.; Chen, N.; Chen, J.; Soo, M. T.; Wood, B.; Yang, D. J.; Du, A. J. et al. Graphene defects trap atomic Ni species for hydrogen and oxygen evolution reactions. *Chem* **2018**, *4*, 285–297.

[23] Yan, X. C.; Jia, Y.; Zhang, L. Z.; Soo, M. T.; Yao, X. D. Defective graphene anchored iron-cobalt nanoparticles for efficient electrocatalytic oxygen reduction. *Chem. Commun.* **2017**, *53*, 12140–12143.

[24] Zhao, X. J.; Zou, X. Q.; Yan, X. C.; Brown, C. L.; Chen, Z. G.; Zhu, G. S.; Yao, X. D. Defect-driven oxygen reduction reaction (ORR) of carbon without any element doping. *Inorg. Chem. Front.* **2016**, *3*, 417–421.

[25] Jia, Y.; Zhang, L. Z.; Du, A. J.; Gao, G. P.; Chen, J.; Yan, X. C.; Brown, C. L.; Yao, X. D. Defect graphene as a trifunctional catalyst for electrochemical reactions. *Adv. Mater.* **2016**, *28*, 9532–9538.

[26] Zhao, H. Y.; Sun, C. H.; Jin, Z.; Wang, D. W.; Yan, X. C.; Chen, Z. G.; Zhu, G. S.; Yao, X. D. Carbon for the oxygen reduction reaction: A defect mechanism. *J. Mater. Chem. A* **2015**, *3*, 11736–11739.

[27] Yang, Q.; Jia, Y.; Wei, F. F.; Zhuang, L. Z.; Yang, D. J.; Liu, J. Z.; Wang, X.; Lin, S.; Yuan, P.; Yao, X. D. Understanding the activity of Co-$N_{4-x}C_x$ in atomic metal catalysts for oxygen reduction catalysis. *Angew. Chem., Int. Ed.* **2020**, *59*, 6122–6127.

[28] Chen, Y. F.; Li, Z. J.; Zhu, Y. B.; Sun, D. M.; Liu, X. E.; Xu, L.; Tang, Y. W. Atomic Fe dispersed on N-doped carbon hollow nanospheres for high-efficiency Electrocatalytic oxygen reduction. *Adv. Mater.* **2019**, *31*, 1806312.

[29] Guo, D. H.; Shibuya, R.; Akiba, C.; Saji, S.; Kondo, T.; Nakamura, J. Active sites of nitrogen-doped carbon materials for oxygen reduction reaction clarified using model catalysts. *Science* **2016**, *351*, 361–365.

[30] Zhou, T. S.; Zhou, Y.; Ma, R. G.; Zhou, Z. Z.; Liu, G. H.; Liu, Q.; Zhu, Y. F.; Wang, J. C. Nitrogen-doped hollow mesoporous carbon spheres as a highly active and stable metal-free electrocatalyst for oxygen reduction. *Carbon* **2017**, *114*, 177–186.

[31] Zhang, L. J.; Su, Z. X.; Jiang, F. L.; Yang, L. L.; Qian, J. J.; Zhou, Y. F.; Li, W. M.; Hong, M. C. Highly graphitized nitrogen-doped porous carbon nanopolyhedra derived from ZIF-8 nanocrystals as efficient electrocatalysts for oxygen reduction reactions. *Nanoscale* **2014**, *6*, 6590–6602.

[32] Liu, W. G.; Zhang, L. L.; Liu, X.; Liu, X. Y.; Yang, X. F.; Miao, S.; Wang, W. T.; Wang, A. Q.; Zhang, T. Discriminating catalytically active FeN_x species of atomically dispersed Fe-N-C catalyst for selective oxidation of the C-H bond. *J. Am. Chem. Soc.* **2017**, *139*, 10790–10798.

[33] Zhou, T. S.; Ma, R. G.; Zhang, T.; Li, Z. C.; Yang, M. H.; Liu, Q.; Zhu, Y. F.; Wang, J. C. Increased activity of nitrogen-doped graphene-like carbon sheets modified by iron doping for oxygen reduction. *J. Colloid Interfaces Sci.* **2019**, *536*, 42–52.

[34] Yun, J. Y.; Hwang, S. H.; Jang, J. Fabrication of Au@Ag core/shell

nanoparticles decorated TiO_2 hollow structure for efficient light-harvesting in dye-sensitized solar Cells. *ACS Appl. Mater. Interfaces* **2015**, *7*, 2055–2063.

[35] Cheng, W. Z.; Yuan, P. F.; Lv, Z. R.; Guo, Y. Y.; Qiao, Y. Y.; Xue, X. Y.; Liu, X.; Bai, W. L.; Wang, K. X.; Xu, Q. et al. Boosting defective carbon by anchoring well-defined atomically dispersed metal-N_4 sites for ORR, OER, and Zn-air batteries. *App. Catal. B: Environ* **2020**, *260*, 118198.

[36] Zhu, A. Q.; Tan, P. F.; Qiao, L. L.; Liu, Y.; Ma, Y. J.; Xiong, X.; Pan, J. Multiple active components, synergistically driven cobalt and nitrogen co-doped porous carbon as high-performance oxygen reduction electrocatalyst. *Inorg. Chem. Front.* **2017**, *4*, 1748–1756.

[37] Zhu, A. Q.; Qiao, L. L.; Tan, P. F.; Ma, Y. J.; Zeng, W. X.; Dong, R.; Ma, C.; Pan, J. Iron-nitrogen-carbon species for oxygen electro-reduction and Zn-air battery: Surface engineering and experimental probe into active sites. *App. Catal. B: Environ.* **2019**, *254*, 601–611.

[38] Yao, Y. G.; Huang, Z. N.; Xie, P. F.; Wu, L. P.; Ma, L.; Li, T. Y.; Pang, Z. Q.; Jiao, M. L.; Liang, Z. Q.; Gao, J. L. et al. High temperature shockwave stabilized single atoms. *Nat. Nanotechnol.* **2019**, *14*, 851–857.